



Nonfluorinated Ionic Liquid Electrolytes for Lithium Metal Batteries: Ionic Conduction, Electrochemistry, and Interphase Formation

Niyousha Karimi, Maider Zarrabeitia, Alessandro Mariani, Daniele Gatti, Alberto Varzi,* and Stefano Passerini*

Cyano-based ionic liquids (ILs) are prime candidates for the manufacturing of cheaper and safer batteries due to their inherently low-volatility and absence of expensive fluorinated species. In this work, *N*-methyl-*N*-butylpyrrolidinium (Pyr₁₄)-based ILs featuring two different cyano-based anions, i.e., dicyanamide (DCA) and tricyanomethanide (TCM), and their mixture with the respective Li salts (1:9 salt:IL mole ratio), alongside their combination (DCA–TCM), are evaluated as potential electrolytes for lithium metal batteries (LMBs). The electrolytes display significant ionic conductivity at room temperature (5 mS cm⁻¹) alongside an electrochemical stability window up to 4 V, suitable for low-voltage LMBs such as Li–sulfur, as well as promising cycling stability. In addition to the detailed physicochemical (viscosity, conductivity) and electrochemical (electrochemical stability window, stripping/plating, and impedance test in symmetrical Li cells) characterization, the solid electrolyte interphase (SEI) formed in this class of ionic liquids is studied for the first time. X-ray photoelectron spectroscopy (XPS) provides evidence for an SEI dominated by a polymer-rich layer including carbon–nitrogen single, double, and triple bonds, which provides high ionic conductivity and mechanical stability, leading to the aforementioned cycling stability. Finally, a molecular insight is achieved by density functional theory (DFT) and classic molecular dynamics simulations both supporting the experimental evidence.

1. Introduction

The increasing demand for electric vehicles is a strong driving force for the development of batteries beyond the state-of-the-art lithium-ion batteries (LIBs) in terms of cost, energy performance and safety.^[1] Moving to cell chemistries based on Li metal anodes, such as Li–S (2567 Wh kg⁻¹) and Li–O₂ (3505 Wh kg⁻¹) batteries, appears to be vital considering energy performance and cost. Lithium exhibits a high theoretical capacity (3861 mAh g⁻¹) and has the most negative redox potential (–3.04 V vs SHE). Nonetheless, this promising anode displays high reactivity toward most electrolytes leading to the formation of an interphase layer at the electrode/electrolyte interface known as the solid electrolyte interphase (SEI). Because the Li metal surface is regenerated upon charging of the cell, the reductive decomposition of the electrolyte may occur in every cycle, leading to the irreversible consumption of both Li and the electrolyte, capacity loss, and inhomogeneous lithium deposition. This latter results in dendrite formation, which may induce internal short circuit and cell failure. In this scenario, the choice of the electrolyte is crucial to ensure


the formation of a uniform, flexible and yet highly ionic conductive SEI layer, which can withstand the extreme conditions occurring at the Li metal interface. Among the several proposed solutions, ionic liquids (ILs)-based electrolytes are capable of forming an interphase with such properties.^[2] Additionally, they feature low flammability, low volatility, and relatively high ionic conductivity.^[3]

Recent studies of bis(trifluoromethanesulfonyl)imide (TFSI)-based and bis(fluorosulfonyl)imide (FSI)-based ILs showed efficient Li stripping/plating behavior.^[2,4] Nevertheless, fluorinated ILs are still relatively expensive and pose concerns about their environmental impact. Therefore, we focused our attention on fluorine-free ILs, combining cyano-based anions (dicyanamide, DCA⁻ and tricyanomethanide, TCM⁻) with the pyrrolidinium cation (shown in **Figure 1**), due to their reduced costs (F-free) and potentially enhanced safety and environmental friendliness.^[4]

In this work mixtures of LiDCA:Py₁₄DCA and LiTCM:Py₁₄TCM as well as LiDCA:Py₁₄TCM electrolytes are

N. Karimi, Dr. M. Zarrabeitia, Dr. A. Mariani, D. Gatti, Dr. A. Varzi, Prof. Dr. S. Passerini
Helmholtz Institute Ulm (HIU) Helmholtzstrasse 11
Ulm 89081, Germany
E-mail: alberto.varzi@kit.edu; stefano.passerini@kit.edu

N. Karimi, Dr. M. Zarrabeitia, Dr. A. Mariani, D. Gatti, Dr. A. Varzi, Prof. Dr. S. Passerini
Karlsruhe Institute of Technology (KIT)
P.O. Box 3640, Karlsruhe 76021, Germany

 The ORCID identification number(s) for the author(s) of this article can be found under <https://doi.org/10.1002/aenm.202003521>.

© 2020 The Authors. Advanced Energy Materials published by Wiley-VCH GmbH. This is an open access article under the terms of the Creative Commons Attribution-NonCommercial-NoDerivs License, which permits use and distribution in any medium, provided the original work is properly cited, the use is non-commercial and no modifications or adaptations are made.

DOI: 10.1002/aenm.202003521

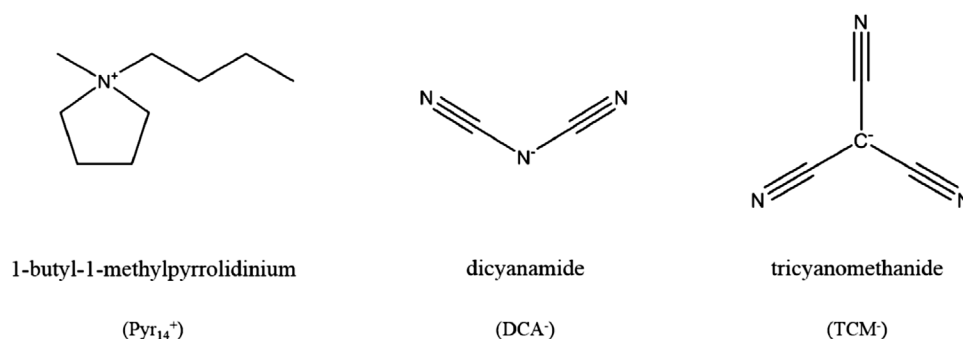


Figure 1. Structures of ions constituting the ILs investigated in this study.

thoroughly studied. The physicochemical and electrochemical properties of DCA⁻ and TCM⁻-based IL electrolytes and their mixture are extensively investigated in terms of viscosity, conductivity, electrochemical stability, and stripping/plating behavior of symmetrical Li/Li cells. In order to comprehensively understand the nature and composition of the formed SEI layer on the lithium metal surface upon cycling, X-ray photoelectron spectroscopy (XPS) was used. Additionally, the evolution of the interphase layer was monitored via electrochemical impedance spectroscopy (EIS). The experimental results were supported by classic molecular dynamics (MD) and density functional theory (DFT) simulations. To date, such a study has not been conducted for LiTCM:Pyr₁₄TCM and LiDCA:Pyr₁₄TCM at all and not for LiDCA:Pyr₁₄DCA to the comprehensive degree reported here.

2. Results and Discussion

2.1. Classic Molecular Dynamics and DFT Simulations

The structure of the solvation shells around the Pyr₁₄⁺ and the two anions DCA⁻ and TCM⁻ was investigated via classic MD simulations by means of radial distribution functions (RDFs, $g(r)$) and spatial distribution functions (SDFs). The snapshots of the final equilibrated systems are depicted in Figure S1 in the Supporting Information. We selected two RDFs for each system, namely the one for the distance between the Li⁺ cation and the anion center of mass (COM), and the one for the distance between the Pyr₁₄⁺ center of ring (COR) and the anion COM. The corresponding results are shown in Figure 2a,b. As it appears clear, DCA⁻ approaches both the cations more closely than TCM⁻. A better view of the three-dimensional molecular arrangement is obtained with the SDFs shown in Figure 2c,d. The cation, Pyr₁₄⁺, appears in both systems closely solvated by anions in an almost isotropic way around the ring, while a second shell made of other cations is composed of Li⁺ and Pyr₁₄⁺ for the DCA-based system, and only of Pyr₁₄⁺ for the TCM-based one. This difference could be explained by the larger coordination number of TCM⁻ (which has ≈ 0.5 Li⁺ cations in its first solvation shell) compared to DCA⁻ (which only has ≈ 0.4). Surprisingly, Li⁺ is found to coordinate TCM⁻ in a tetrahedral fashion, while it interacts in-plane with DCA⁻ and not with the central nitrogen atom.

In order to explore the electronic properties of the electrolytes, we performed also DFT calculations on both the single anions and some selected clusters of anions and Li⁺ cations. From the optimized geometries of the single anions it is

possible to have an insight on the electron distribution and, consequently, charge delocalization. Both DCA⁻ and TCM⁻ in their singlet form show a clear negative charge accumulation on the nitrogen atoms, as expected from electronegativity considerations (see Figure S2 in the Supporting Information). Even if both the anions have the same number of nitrogen atoms the negative charge accumulation in DCA⁻ is more pronounced than in TCM⁻. The lesser negative charge density on TCM⁻ is easily explained considering the major extension of the conjugated molecular orbitals, which can more easily accommodate the negative charge. When an extra electron is injected in the system forming the radical di-anion, i.e., the doublet form, the two net negative charges increase dramatically the electron density in both species (see Figure 3 inset). Remarkably DCA⁻ loses completely any region of positive or neutral charge. Interestingly, however, a clear negative charge emerges on the central carbon atom of TCM⁻ (Figure 3b, inset), while the nitrile carbon atoms keep their neutrality to some extent.

Finally, we considered clusters with a general composition [Li₅ Anion₂] in both singlet and doublet form with an overall charge of +3 or +2, respectively, shown in Figure 3. While a mostly ordered structure is found in both the singlet clusters, a much more complex arrangement is observed in the doublet clusters. In fact, with both the anions it is possible to clearly see the incipient formation of Li₃N, with consequent hybridization change of the nitrile carbon atom from sp¹ to sp², evidenced by the N–C–N and C–C–N angles for DCA⁻ and TCM⁻, respectively. In fact, these angles change from $\approx 180^\circ$, typical of sp¹ hybridization, to 130° – 140° , i.e., much closer to the theoretical 120° proper of the sp² carbon.

In the TCM⁻ cluster, an additional interesting point is the polymerization of the anions by the formation of a new N–C bond. The same was not observed to occur in the DCA⁻ cluster probably because of the relative orientation of the molecules in the starting geometry and/or because the model is considered to be isolated in the gas phase. The role of other species (Pyr₁₄⁺, other Li⁺, and other anions) will be better explored in a forthcoming work.

2.2. Physicochemical Characterization

Figure 4 summarizes the physicochemical characteristics of the investigated ILs, namely, Pyr₁₄DCA and Pyr₁₄TCM, and their binary solutions with the respective Li salts in the 1:9 salt:IL mole ratio.

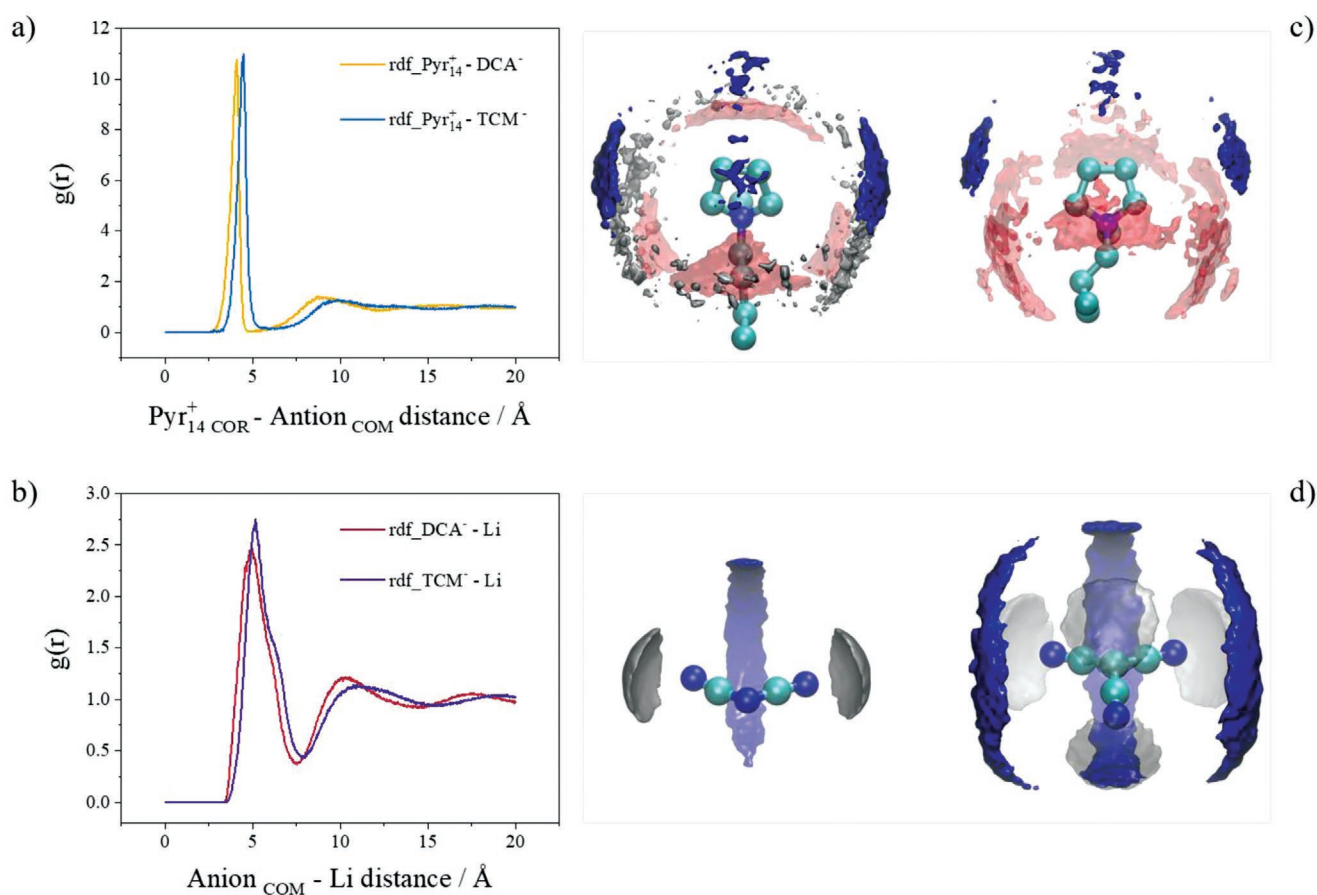


Figure 2. Solvation shell analysis from the MD simulations. a) Radial distribution function of the Pyr_{14}^+ COR and DCA^- COM (yellow) or TCM^- COM (blue). b) Radial distribution function of Li^+ and DCA^- COM (red) or TCM^- COM (purple). c) Spatial distribution function referenced to a central Pyr_{14}^+ (hydrogen atoms are not shown for clarity), anion (red), cation (blue), and Li^+ (silver). The left and right images refer to DCA^- and TCM^- -containing systems, respectively. d) Spatial distribution function referenced to a central anion, color scheme is the same as panel (c).

Figure 4a reports the ionic conductivity versus temperature. At 20 °C the $\text{Pyr}_{14}\text{DCA}$ and $\text{Pyr}_{14}\text{TCM}$ display ionic conductivity of 10.7 and 8.6 mS cm^{-1} , respectively. These values are well above those of their fluorinated analogues (e.g., $\text{Pyr}_{14}\text{TFSI}$: 1.8 mS cm^{-1} at 20 °C).^[5] Figure 4b displays the viscosity of the pure ILs in the temperature range from 0 to 50 °C showing that $\text{Pyr}_{14}\text{DCA}$ has a higher viscosity than $\text{Pyr}_{14}\text{TCM}$, i.e., 38.1 and 33.1 mPa s at 20 °C, respectively. According to the Walden's rule (Equation (1)), a correlation between the logarithm of the molar conductivity and the logarithm of fluidity (inverse of viscosity) is expected^[6]

$$\Lambda \eta^\alpha = C \quad (1)$$

where Λ is the molar conductivity, η is the viscosity, C is the temperature-dependent constant, and α is the decoupling constant corresponding the slope of the Walden plot. Figure 4c shows the Walden plot of the investigated ILs and electrolytes, in which the reference ideal behavior line is represented by the 1 M KCl. As expected both $\text{Pyr}_{14}\text{DCA}$ and $\text{Pyr}_{14}\text{TCM}$ obey the

Walden rule and lie below the ideal line. Nevertheless, the α values obtained are less than 1, indicating that the activation energy for the viscous flow in both ILs is higher than that of the conductive flow. Considering the vertical distance between the ideal line and each system, i.e., ΔW , it is possible to estimate the amount of nonclosely paired ions or the so called ionicity following Equation (2)^[7]

$$I_w = 10^{-\Delta W} \quad (2)$$

The ionicity values obtained for the $\text{Pyr}_{14}\text{DCA}$ and $\text{Pyr}_{14}\text{TCM}$ are 83% and 66%, respectively. To explain the counter-intuitive behavior of $\text{Pyr}_{14}\text{DCA}$ in comparison to $\text{Pyr}_{14}\text{TCM}$ (i.e., the former is both more viscous and more ionic conductive) MD simulation of 500 ps dumped every 50 fs was performed, through which the lifetime of the ion pairs could be calculated via autocorrelation functions.^[8,9,10] Interestingly, the estimated ion pairs lifetime for $\text{Pyr}_{14}\text{DCA}$ and $\text{Pyr}_{14}\text{TCM}$ were ≈ 10.06 and ≈ 6.04 ps, respectively. Nevertheless, the average number of the ion pairs was noticeably larger in the latter. These findings reflect very well the experimental observation of higher

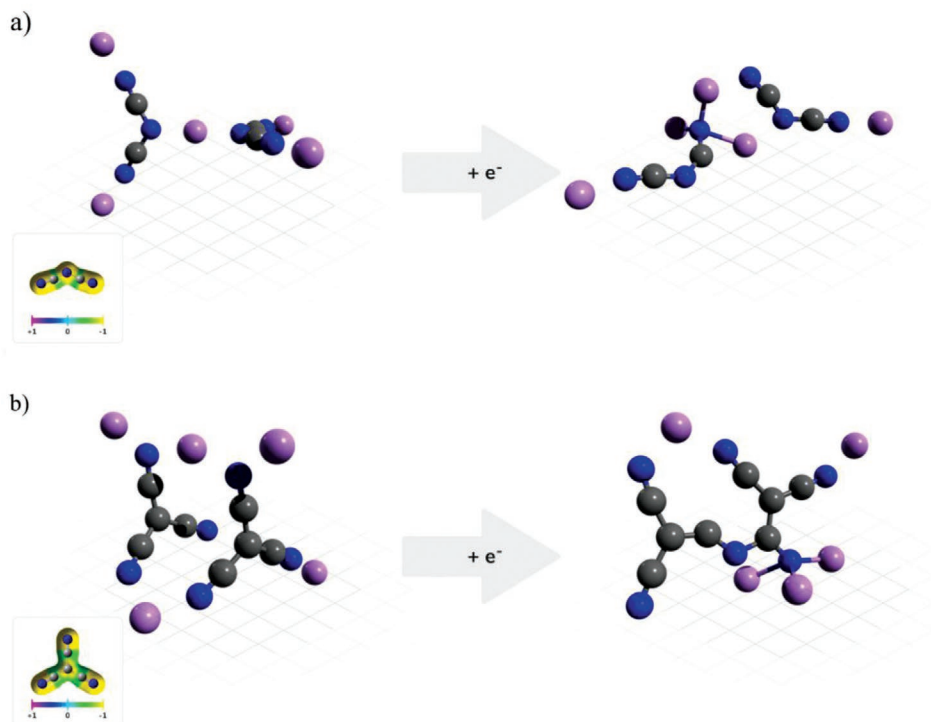


Figure 3. DFT optimized geometries for: a) $[\text{Li}_5\text{DCA}_2]$ and b) $[\text{Li}_5\text{TCM}_2]$. For both the panels the images on the left and the right illustrate the singlet and the doublet form, respectively. In the inset the electrostatic potential surface is shown.

viscosity for $\text{Pyr}_{14}\text{DCA}$ (more durable ion pairs), together with its higher conductivity (less ion pairs). Similar discrepancy have been observed in other ILs in molten state,^[11–13] which are attributed to the formation of complex species including ion pairs and/or aggregations, indicating that the conductive and structural modes of motion are not completely coupled.^[14]

The addition of the Li salt results in decreased ionic conductivity and increased viscosity values with respect to the neat ILs. In a salt-IL solution, the higher surface charge density of the small Li^+ (compared to Pyr_{14}^+) leads to a stronger anion- Li^+ interaction, increasing the viscous drag and reducing ionic conductivity.^[15] As shown in Figure 4a,b, $\text{LiDCA}:\text{Pyr}_{14}\text{DCA}$ displays ionic conductivity and viscosity of 5.3 mS cm^{-1} and 84.2 mPa s at 20°C , respectively. However, the TCM-based electrolyte, i.e., $\text{LiTCM}:\text{Pyr}_{14}\text{TCM}$, shows less change with respect to the neat IL, with ionic conductivity of 5.7 mS cm^{-1} and viscosity of 52.0 mPa s at 20°C . Larger decrease in ionic conductivity of DCA-based electrolyte can be well explained by the MD simulation results (see Section 2.1) and Walden plot because of the decreased number of charge carriers per unit of volume.

Despite the decrease in ionic conductivity after addition of the salt, the obtained values are still well above those of the current state-of-the-art, fluorinated IL-based electrolytes (e.g., $\text{LiTFSI}:\text{Pyr}_{14}\text{TFSI}$ (1:9 mol:mol): 1.1 mS cm^{-1} at 20°C).^[16] Therefore, both the DCA- and the TCM-based electrolytes appear suitable for use in batteries.

Figure 4d,e shows the linear sweep voltammeteries of the neat $\text{Pyr}_{14}\text{TCM}$ and $\text{Pyr}_{14}\text{DCA}$, as well as their binary electrolytes, namely, $\text{LiTCM}:\text{Pyr}_{14}\text{TCM}$ and $\text{LiDCA}:\text{Pyr}_{14}\text{DCA}$ (1:9 mol:mol). All potentials are given versus the Li/Li^+ redox

couple. As demonstrated in Figure 4d,e, the current evolution upon the cathodic scan for both the neat ILs is very similar. Starting from OCV, the first reduction wave appears at 1.9 V for $\text{Pyr}_{14}\text{DCA}$ and 1.8 V for $\text{Pyr}_{14}\text{TCM}$. This is then followed by a severe reduction peak appearing slightly above 1 V (at $\approx 1.1 \text{ V}$). The similar reduction pattern for both $\text{Pyr}_{14}\text{TCM}$ and $\text{Pyr}_{14}\text{DCA}$ ILs was expected, considering the predominant role of the organic cation reduction in determining the cathodic limit of neat ILs.

The corresponding anodic scan of neat $\text{Pyr}_{14}\text{TCM}$ reveals a current increase with onset at 3.5 V and reaching the current threshold of $10 \mu\text{A cm}^{-2}$ at 4.0 V . The curve recorded for neat $\text{Pyr}_{14}\text{DCA}$ shows a negligible background current (below $2 \mu\text{A cm}^{-2}$) starting from OCV, reaching the main oxidation peak at 3.5 V . It is worth noting the difference in the behavior of the two ILs as they reach the $10 \mu\text{A cm}^{-2}$ current limit. In fact, the current shows a continuous increase for $\text{Pyr}_{14}\text{TCM}$, in contrast to the decrease to lower values for $\text{Pyr}_{14}\text{DCA}$, indicating partial passivation of the Pt electrode surface. This suggests that the two ILs follow different oxidation pathways. Macfarlane et al. previously reported similar anodic features in electrochemical oxidation of 1-ethyl-3-methylimidazolium dicyanamide (Emim DCA), attributed to the formation of a neutral dimer $(\text{CN})_2\text{N}-\text{N}(\text{CN})_2$,^[17,18] whereas the TCM^- anions were shown to form tricyanocarbonium $\text{C}(\text{CN})_3^+$ ions via removal of two electrons in presence of a strong oxidizing agent.^[19]

The effect of salt addition on the electrolytes ESW is also reported in Figure 4d,e. Upon the anodic scan of both $\text{LiTCM}:\text{Pyr}_{14}\text{TCM}$ and $\text{LiDCA}:\text{Pyr}_{14}\text{DCA}$ the current reaches

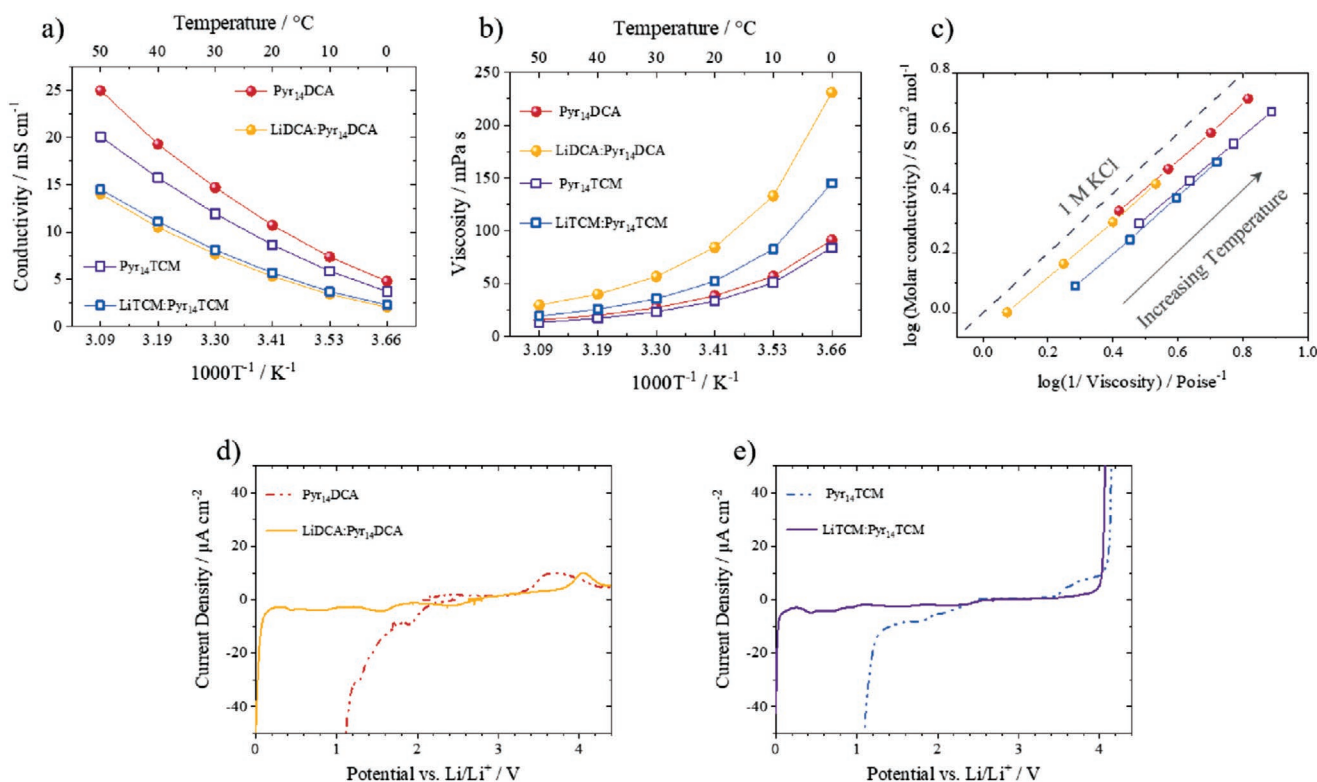


Figure 4. Top: a) Ionic conductivity and b) viscosity versus temperature plots of neat Pyr₁₄DCA, neat Pyr₁₄TCM and LiDCA:Pyr₁₄DCA, LiTCM:Pyr₁₄TCM electrolytes in 1:9 mol salt:IL ratio. Temperature range 0 to 50 °C with heating rate of 5 °C h⁻¹. c) Walden plot of neat Pyr₁₄DCA, neat Pyr₁₄TCM and LiDCA:Pyr₁₄DCA, LiTCM:Pyr₁₄TCM electrolytes in 1:9 mol salt:IL ratio. Bottom: Linear sweep voltammograms of Li/IL/Pt cells recorded at scan rate of 1 mV s⁻¹ at 20 °C, d) neat Pyr₁₄DCA and LiDCA:Pyr₁₄DCA (1:9 mol:mol), and e) neat Pyr₁₄TCM and LiTCM:Pyr₁₄TCM (1:9 mol:mol).

the limit of 10 $\mu\text{A cm}^{-2}$ at 4 V, displaying an almost similar trend to their neat IL counterpart. Differently, the addition of Li salt substantially improves their cathodic stability. The extensive reduction peak at ≈ 1 V is converted to small reduction waves while the cathodic limit of both electrolyte solutions is extended to ≈ 0 V. This is indicative of reactions occurring prior to decomposition of Pyr₁₄⁺, which passivate the electrode surface thus strongly limiting the electrolyte decomposition. Similar effects, highlighting the paramount role of Li salt on the improvement of cathodic stability of IL, have also been observed by other authors.^[20–26] The extended cathodic limit compared to the neat IL could be attributed to the partial charge transfer of the anion on the small Li⁺ ions, reducing electron density of the anion (in this case DCA⁻ or TCM⁻). Such strong Coulombic interaction between the Li⁺ and the anion can in turn cause the reduction of the anion to form a stable Li-ion conducting passivation layer on the electrode surface (Pt or Li metal) preventing the severe reduction/decomposition of the organic cation (Pyr₁₄⁺).^[26]

In general, cyano-based ILs feature lower anodic stability in comparison to the state-of-the-art TFSI⁻ based ILs, due to the absence of electron-withdrawing fluorines in the anions. However, considering the ESW of 4 V, the high ionic conductivity, low density,^[17,27] and lower production costs and toxicity, both TCM-based and DCA-based ILs can be considered as suitable electrolytes for battery applications incorporating low voltage cathodes such as sulfur (Li–S batteries) or LiFePO₄.

2.3. Electrochemical Performance of Li Symmetrical Cells

The compatibility of the electrolytes with lithium metal was investigated performing stripping/plating tests of symmetrical Li/Li cells. The cells were cycled at a current density of 0.05 mA cm⁻² for 1 h for each polarization, while impedance spectra were measured right before the test started (i.e., after the initial 10 h rest) and every 24 h during cycling. The voltage profiles displayed in **Figure 5a** show the direct comparison of the stripping/plating behavior in TCM- and DCA-based electrolytes. The cell employing LiTCM-Pyr₁₄TCM electrolyte (purple line), displayed an initial polarization of $\approx \pm 35$ mV, which gradually increased to $\approx \pm 65$ mV over the course of the experiment. Moreover, the measurement showed a steady, flat polarization profile upon time, further evidenced by the magnification of the voltage profile reported in the insets of **Figure 5a**, suggesting a very stable Li/TCM-based electrolyte interface upon stripping/plating. In case of LiDCA-Pyr₁₄DCA (yellow line), the initial overpotential of $\approx \pm 90$ mV is more than twice that observed for the TCM-based electrolyte. Nevertheless, in DCA-based electrolyte the cell polarization only increases of ≈ 10 mV upon stripping/plating, reaching $\approx \pm 100$ mV during the 230 h of cycling.

The Nyquist plots of the symmetrical Li/Li cells employing TCM-based and DCA-based electrolytes are shown in **Figure 5b,c**, respectively. The interfacial resistance (R_{int}) was calculated by summing the charge transfer resistance (R_{CT}) and the SEI layer resistance (R_{SEI}). Since the focus of this study is

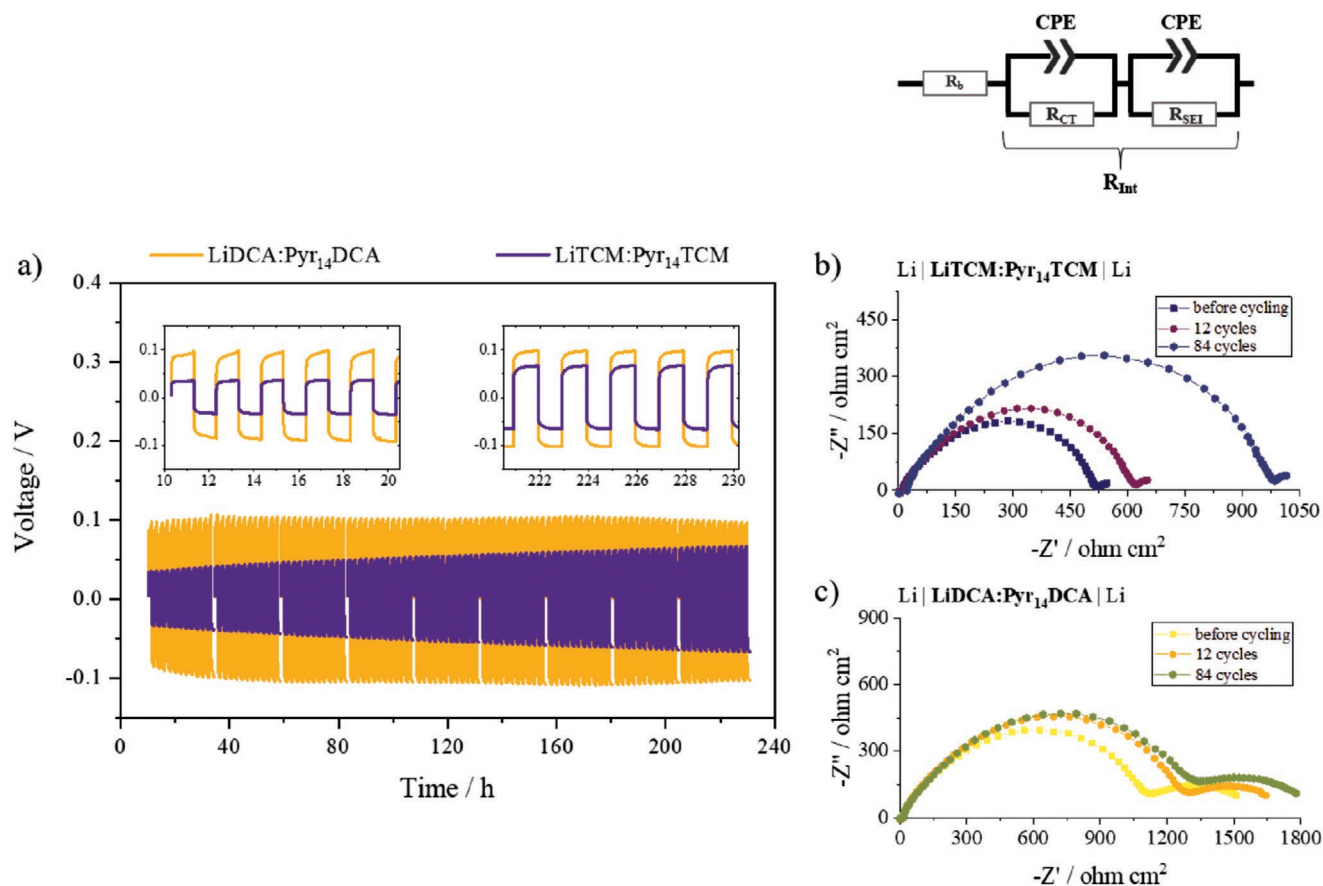


Figure 5. a) Time evolution of the cell voltage and, in inset, magnification of the first 10 h and last 10 h of cycling during stripping/deposition measurements performed on symmetrical Li/electrolyte /Li cells using a current of 0.05 mA cm^{-2} and a deposition/stripping time of 1 h. Right: Nyquist plots of a symmetrical Li/IL-based electrolyte/ Li cells upon time. Specifically, after 10 h rest prior to cycling, after 12 cycles and after 84 cycles, b) LiTCM:PyT₁₄TCM electrolyte, and c) LiDCA:PyT₁₄DCA.

the interphase, for sake of simplicity, the diffusive part of the spectra at low frequency was not included in the fitting of the impedance data. The impedance fitting parameters are presented in Table S1 (Supporting Information).

In agreement with the stripping/plating tests, the interfacial resistance for the TCM-based cell (Figure 5b) remained lower than that of the DCA-based cell both before and after the cycling test, which may suggest for the formation of a thinner and/or more conductive SEI with the TCM-based electrolyte. The interfacial resistance in TCM-based cell before cycling (i.e., only upon contact with the electrolyte) was around $502 \Omega \text{ cm}^2$. After 84 cycles of stripping/plating it increased to around $954 \Omega \text{ cm}^2$. Differently, the interfacial resistance in DCA-based cell was substantially higher in the beginning (around $1084 \Omega \text{ cm}^2$), but then only increased slightly after 84 cycles (to $\approx 1280 \Omega \text{ cm}^2$). Such results suggest that the SEI layer in this case is mostly forming during the rest time. In fact, the DFT calculations (see Section 2.1) showed that the injection of an extra electron in DCA⁻ causes the spin-density around the terminal nitrogen atoms to be anisotropic (see Figure S3 in the Supporting Information), with a lower-density region located between the two nitrile groups. This peculiar charge distribution makes the DCA⁻ more prone to be electrophilically attacked on the opposite side. On the other hand, the more symmetrical structure

of TCM⁻ makes the distribution of the extra electron more isotropic.

It should be noted that in a recent study on the applications of DCA-based IL for LIBs, Yoon et al. proposed that achieving an optimum cycling ability requires the moisture content to be carefully controlled.^[4] To illustrate this, they conducted stripping/plating cycling tests on symmetrical Li cells including electrolytes with moisture content varying from 36 to 443 ppm. An overpotential of about 4 V was observed at the lowest moisture content, causing cycling failure in the cell, while optimum behavior was observed with 200 ppm of water. This is in contradiction with our results, being able to perform stripping/plating experiments with a moisture content below 20 ppm. A possible reason might be the different drying method. In fact, Yoon et al. eliminated moisture from the electrolyte by contacting it with lithium metal for up to three months, resulting in noticeable color change. It cannot be excluded that the formation of the SEI on the lithium metal altered the nature of the IL they investigated.

2.4. Solid Electrolyte Interphase Characterization

In order to understand the differences between the SEI formed in the cyano-based electrolytes, the surface of lithium metal

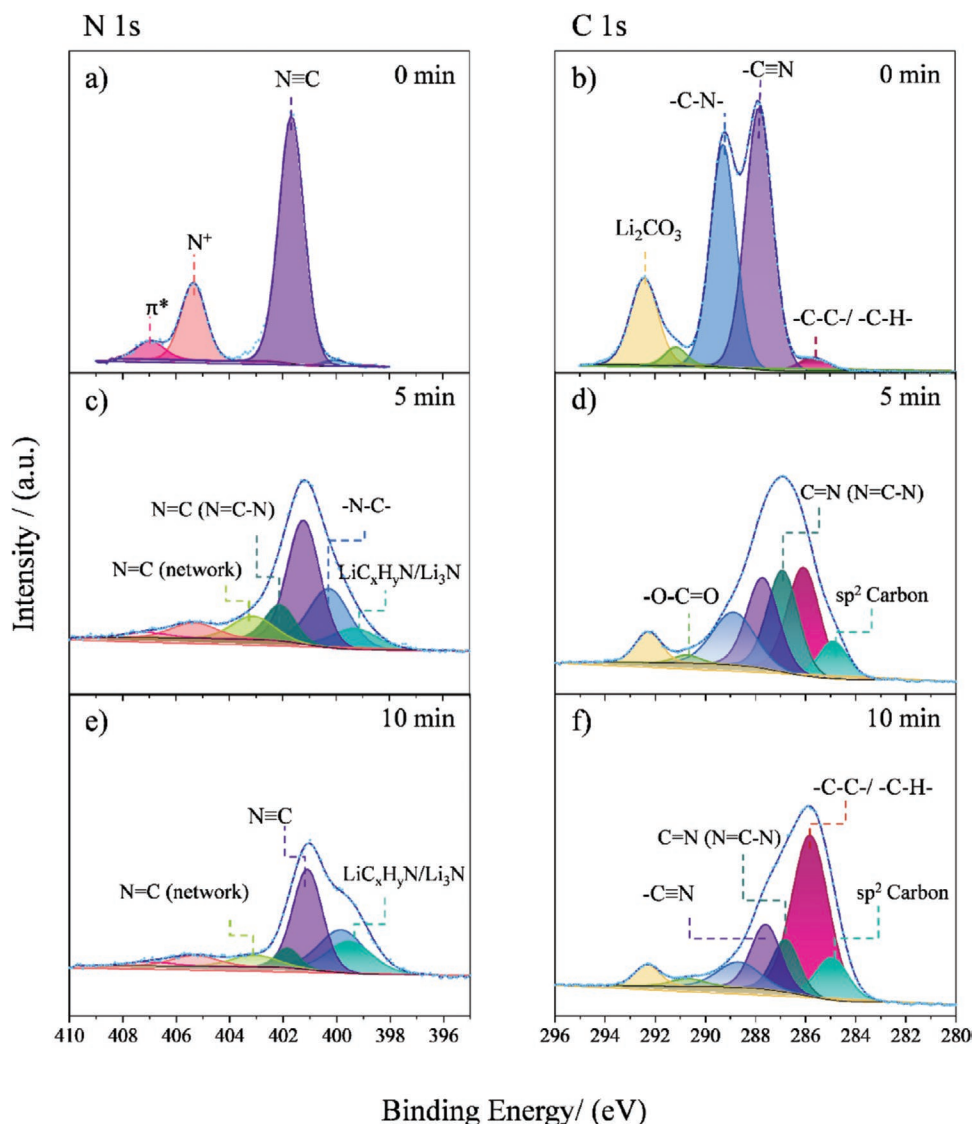


Figure 6. High-resolution N 1s, and C 1s photoelectron spectra, before and after etching, of the Li metal surface after the first lithium plating (current: 0.05 mA cm^{-2} , plating time 1 h) in LiTCM:Py₁₄TCM (1:9 mol:mol).

electrodes after the first deposition step was studied by means of XPS. To provide more insights into the nature of the SEI layer, the samples were also etched by argon ions sputtering, acquiring high resolution region spectra after 5 and 10 min for each sample (for DCA sample additional 20 min of ion sputtering was needed). The XPS spectrum of pristine Li metal is also shown in Figure S4 as reference. It should be noted that due to surface charging, which is inherent to electronically insulating material, the calibration of the XPS data using the $-\text{C}-\text{C}-\text{sp}^3$ at 284.6 eV as reference was not possible. Instead, all peak assignments were carried out by considering the characteristic BE separations (ΔBEs) between the relevant core levels for specific species (see the Table S2 in the Supporting Information where the experimental BE and the ΔBEs are provided).

Figures 6 and 7 display the N 1s and C 1s core spectra of Li metal electrodes cycled in LiTCM-Py₁₄TCM and

LiDCA-Py₁₄DCA electrolytes, respectively. Besides, Figures S5 and S6 (Supporting Information) show the O 1s and Li 1s regions.

2.4.1. SEI Composition in LiTCM-Py₁₄TCM Electrolyte

The N 1s high-resolution photoelectron spectrum (Figure 6a) from the outermost surface of the cycled Li, display two main components identified as $-\text{C}\equiv\text{N}$ (TCM⁻, $\Delta\text{BE}_{(\text{N } 1\text{s}-\text{C } 1\text{s})} = 113.8 \pm 0.02 \text{ eV}$)^[28–32] and N^+ (Py₁₄⁺, $\Delta\text{BE}_{(\text{N } 1\text{s}-\text{C } 1\text{s})} = 116.0 \pm 0.01 \text{ eV}$)^[33,34] (note that ΔBEs were calculated to confirm the assignment of the species as previously was performed for Li compounds—more details in Table S2 of the Supporting Information). This indicates that despite the washing procedure the IL was still present on the sample surface in a rather significant amount.^[34] The presence of triple $-\text{C}\equiv\text{N}$ bonds is also testified by the observed

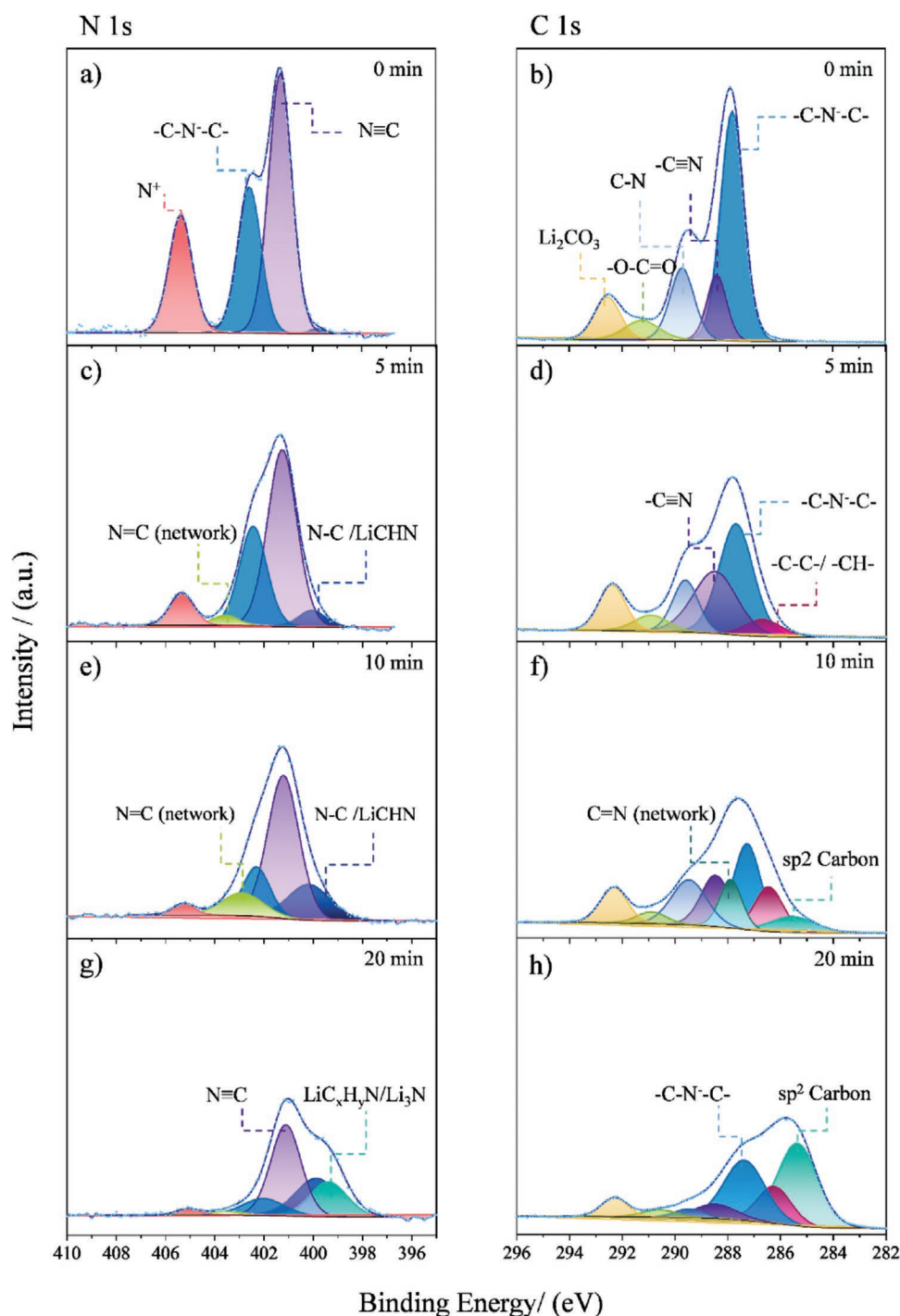


Figure 7. High-resolution N 1s, and C 1s photoelectron spectra, before and after etching, of the Li metal surface after the first lithium plating step (current: 0.05 mA cm^{-2} , plating time 1 h) in LiDCA:Py₁₄DCA (1:9 mol:mol).

feature corresponding to π excitation appearing at a higher BE value of about $\approx 5 \text{ eV}$ with respect to $-\text{C}\equiv\text{N}$ (TCM⁻).^[30]

The C 1s spectra (Figure 6b) reveals the presence of species containing $-\text{C}-\text{C}-/\text{-C}-\text{H}-$, $-\text{C}\equiv\text{N}$ and, $-\text{C}-\text{N}-$ bonds (appearing in order of increasing BEs),^[28–30] which are mostly originating from the IL persisting on the surface. Additionally, peaks attributed to Li_2CO_3 ($\Delta\text{BE}_{(0 \text{ 1s}-\text{C} \text{ 1s})} = 241.9 \pm 0.06 \text{ eV}$)^[35]

and species with $-\text{O}-\text{C}=\text{O}$ character (possibly lithium alkyl carbonate, O 1s–C 1s separation $\Delta\text{BE} = 244.6 \pm 0.08 \text{ eV}$ ^[34]) were also detected. These features could arise from the reaction of lithium metal (not coated by the SEI) with DMC during the washing step or from the native film persisting on the lithium surface (as shown by the XPS spectra in Figure S4 of the Supporting Information).

After 5 min of etching, both main peaks of N 1s and C 1s spectra (Figure 6c,d) shift to lower binding energies, demonstrating a different composition of the outermost surface with respect to inner layer. The amount of the $-\text{C}\equiv\text{N}$ ($\Delta\text{BE}_{(\text{N } 1\text{s}-\text{C } 1\text{s})} = 113.5 \pm 0.09$ eV) and N^+ ($\Delta\text{BE}_{(\text{N } 1\text{s}-\text{C } 1\text{s})} = 116.4 \pm 0.01$ eV) present in the sample decreases significantly, in agreement with the IL being mostly on the sample's surface. Meanwhile, the intensity of peaks corresponding to the reduction products of both cation and anion increases. Indeed, the peaks attributed to $-\text{C}-\text{N}$ and/or LiCHN ($\Delta\text{BE}_{(\text{N } 1\text{s}-\text{C } 1\text{s})} = 111.3 \pm 0.06$ eV)^[28-30,36] and $-\text{C}=\text{N}$ bonds ($\Delta\text{BE}_{(\text{N } 1\text{s}-\text{C } 1\text{s})} = 115.1 \pm 0.1$ eV)^[28-30,36] evolve after 5 min of etching. It should be noted that in the N 1s spectrum two separate peaks associated with $-\text{C}=\text{N}$ bonds could be identified, one belonging to $-\text{C}=\text{N}$ bonds in a polymeric network and one in $-\text{C}=\text{N}-\text{C}-$ configuration (the latter appearing at lower binding energy).^[30,37] These peaks, which result from decomposition/trimerization of TCM-based IL^[34-39] are not distinguished as two separate features in C 1s spectrum, due to the high amount of species observed in a small range of BE. Furthermore, the N 1s spectrum shows a small peak at lowest BE, which is characteristic of $\text{LiC}_x\text{H}_y\text{N}/\text{Li}_3\text{N}$ species ($\Delta\text{BE}_{(\text{N } 1\text{s}-\text{Li } 1\text{s})} = 341.8 \pm 0.02$ eV).^[35,36] The formation of such species can be supported by the observed graphitic sp^2 carbon peak appearing at about ≈ 0.8 eV lower than $-\text{C}-\text{C}-/\text{C}-\text{H}-$ peak (Figure 6d), possibly indicating the complete reduction of TCM⁻ anion as supported by our DFT calculations (see Figure 3b) and also previously proposed by Zhang et al.^[37]

After 10 minutes of sputtering, the N^+ peak corresponding to the IL cation is still observed (see Figure 6e), suggesting that the IL is not only on the surface, but also physically trapped within the SEI layer structure. Furthermore, as shown in Figure 6d,e, the intensity of the peaks associated with carbon and nitrogen atoms having single, double and triple bonds further decrease compared to the spectra obtained after 5 min of etching. Exceptions are the $\text{LiC}_x\text{H}_y\text{N}/\text{Li}_3\text{N}$ peak in N 1s spectrum and the sp^2 and sp^3 carbon peaks in C 1s region, which display a further increase. This increase could be indicative of the severe reduction of both Pyr_{14}^+ and TCM⁻ at more reducing environments in the proximity of the metallic lithium surface.

2.4.2. SEI Composition in LiDCA-Pyr₁₄DCA Electrolyte

The N 1s high-resolution photoelectron spectrum at the surface of Li after one deposition step in LiDCA-Pyr₁₄DCA (Figure 7a) displays three main peaks. The first two are associated with DCA⁻ anion, namely, $-\text{C}\equiv\text{N}$ ($\Delta\text{BE}_{(\text{N } 1\text{s}-\text{C } 1\text{s})} = 112.9 \pm 0.07$ eV) and $\text{C}-\text{N}^--\text{C}$ ($\Delta\text{BE}_{(\text{N } 1\text{s}-\text{C } 1\text{s})} = 114.7 \pm 0.07$ eV) while the third peak corresponds to N^+ from Pyr_{14}^+ ($\Delta\text{BE}_{(\text{N } 1\text{s}-\text{C } 1\text{s})} = 115.6 \pm 0.05$ eV). This indicates the presence of remaining IL on the surface of the SEI layer despite the washing, as it also occurred with the TCM-based electrolyte. The C 1s region spectrum (Figure 7b) displays peaks corresponding to $\text{C}-\text{N}$ and $-\text{C}\equiv\text{N}$ as well as Li_2CO_3 and alkyl carbonate ($\Delta\text{BE}_{(\text{O } 1\text{s}-\text{C } 1\text{s})}$ equal to 241.8 ± 0.08 and 244.2 ± 0.06 eV, respectively). It should be noted that the quantity of these two latter species, which are associated with the native surface species and/or the reaction of the Li surface with DMC during the washing, are observed in much less extent than in the TCM-case, suggesting a higher coverage of

the lithium metal surface by decomposition species from IL in the case of DCA-based electrolyte.

After 5 minutes of argon ion sputtering, the IL was only partially removed, as the peak corresponding to N^+ of Pyr_{14}^+ is still observed. Furthermore, in both N 1s and C 1s region spectra (Figure 7c,d), the decomposition products of the Pyr_{14}^+ cation could be noticed, despite the dominating presence of DCA⁻ anion (i.e., $-\text{C}\equiv\text{N}$ and $\text{C}-\text{N}^--\text{C}$). Decomposition of the Pyr_{14}^+ cation is evident by the $-\text{C}-\text{N}-$ (and/or LiCHN) peak ($\Delta\text{BE}_{(\text{N } 1\text{s}-\text{C } 1\text{s})} = 110.4 \pm 0.06$ eV) and $-\text{C}-\text{C}-/\text{C}-\text{H}-$ bonds in N 1s and C 1s regions, respectively. After 10 min etching, in contrast with the observation in TCM-based electrolyte, in both N 1s (Figure 7e) and C 1s (Figure 7f) photoelectron regions no significant changes can be observed, suggesting that the formed SEI layer is thicker and hence more sputtering time is needed to reach the inner part of the SEI. As shown in Figure 7e,f, peaks associated with $-\text{C}\equiv\text{N}$ ($\Delta\text{BE}_{(\text{N } 1\text{s}-\text{C } 1\text{s})} = 112.7 \pm 0.08$ eV) and $-\text{C}-\text{N}^--\text{C}-$ ($\Delta\text{BE}_{(\text{N } 1\text{s}-\text{C } 1\text{s})} = 115.0 \pm 0.09$ eV) are still present as the main components, while the features belonging to the decomposition products only slightly increased. Nonetheless, an interesting phenomenon is observed after 10 min etching, the N 1s spectrum exhibits the signature of a polymeric network of conjugated $-\text{C}=\text{N}$ bonds formed by reduction of DCA⁻ anions.^[38,40] This network appears to be mostly in the inner part of the SEI layer.

To gain further insight into the inner composition of the SEI layer forming in the DCA-based electrolyte, the surface was sputtered for additional 10 min (in total 20 min). Surprisingly, the N 1s spectrum displays extremely similar characteristics to that obtained for the Li plated in TCM-based electrolyte after 10 min of sputtering. The N 1s spectrum (Figure 7g) displays an increased intensity of $-\text{C}-\text{N}-/\text{LiCHN}$ ($\Delta\text{BE}_{(\text{N } 1\text{s}-\text{C } 1\text{s})} = 110.4 \pm 0.07$ eV) associated with decomposition of Pyr_{14}^+ cation. In addition, a new peak attributed to $\text{LiC}_x\text{H}_y\text{N}/\text{Li}_3\text{N}$ ($\Delta\text{BE}_{(\text{N } 1\text{s}-\text{Li } 1\text{s})} = 341.5 \pm 0.1$ eV) appears with a larger intensity with respect to the TCM-based system, whereas the intensity of the peaks corresponding to other species, such as $-\text{C}\equiv\text{N}$, $-\text{C}-\text{N}^--\text{C}$, polymeric $\text{C}=\text{N}$ network and N^+ decrease. This suggests that in the inner part of the SEI some trapped IL is present. Additionally, in C 1s photoelectron region (Figure 7h) the peak associated with sp^2 carbon dominates the spectrum suggesting also for the severe reduction of the IL contributing to the formation of the inner part, i.e., closer to the Li metal surface—of the SEI layer. Overall, these results suggest that the SEI layer formed on Li in DCA-based electrolyte is thicker than that formed in the TCM-based electrolyte, since more sputtering time was required to access the $\text{LiC}_x\text{H}_y\text{N}$ species formed close to the Li metal surface. This claim is also supported by the computational and EIS results previously discussed.

2.4.3. SEI Layer Formation in Cyano-Based Electrolytes

In literature, there are several reports on the use of cyano-based ILs as precursors for the synthesis of nitrogen-enriched carbons.^[39,41,42] In fact, this class of ILs are known for their crosslinking ability upon heat treatment. However, a more detailed study on polymerization of the cyano-based anions carried out by Wooster et al.^[40] showed it to occur only in the

presence of N-containing cations, proposing that the decomposition products of the cation play a key role in initiating the polymerization of the cyano-containing anions.

According to our results, we believe that two factors play the main role in the formation and development of the SEI layer, one being the stability of the electrolyte in contact with metallic lithium and the other being the extent of sp^2 carbon present in the SEI layer composition which can induce catalytic decomposition of the electrolyte.

Although both DCA^- and TCM^- have similar structure and are paired with the same cation (Pyr_{14}^+), the decomposition of the DCA-based electrolyte mostly occurs during the rest time, as evidenced by the EIS measurement (see Section 2.3). The lesser stability of DCA^- is also indicated by the MD and DFT simulation results showing DCA^- to approach both cations (i.e., Pyr_{14}^+ and Li^+) more closely, i.e., being more exposed to the consequent radical reactions. Moreover, the vicinity of Li^+ ions facilitates the formation of the degradation product. Such vicinity can also explain the XPS experimental evidence of larger Li_3N for this electrolyte.

On the other hand, the more symmetrical structure of TCM^- results in a more isotropic distribution of the charge preventing the spontaneous decomposition of the anion. Therefore, the decomposition of Pyr_{14}^+ , occurring prior to the anion's degradation, initiates the polymerization of TCM^- passivating the lithium surface and resulting in a thinner SEI. Moreover, according to the XPS results, the thick SEI layer formed in the DCA-based electrolyte displays a higher fraction of graphitic carbon in the inner layer (with total atomic concentration of 9.4% in DCA-based versus 2.4% in TCM-based electrolyte in the sample). Interestingly, the formation of sp^2 -carbon was also suggested by the DFT calculations (see Section 2.1). Considering the high electronic conductivity of graphitic carbon, this could potentially promote the further electrochemical reduction of the IL contributing to the SEI's thickening.

Regarding the extent of the polymerization and the composition of the SEI, Zhang et al.^[37] have recently reported a surface study of deposited Li on copper foil using LiTCM dissolved in 1,2-dimethoxyethane (DME) as electrolyte. According to their findings, TCM^- forms a polymeric $-C=N$ network on the Li surface. They additionally proposed that LiTCM undergoes an extra reduction step, forming Li_3N and a graphene network in the inner part of the SEI. Although our results cannot entirely explain the exact reduction mechanism, they agree with these findings.

On the basis of the XPS analysis herein performed (detailed summary shown in Figure S7 in the Supporting Information), it can be concluded that the SEI formed in the TCM-based electrolyte consists of two main layers. The outermost layer (i.e., close to the electrolyte) is reach of polymeric species, including groups with carbon–nitrogen single, double, and triple bonds, which ensures a more cohesive and flexible surface film. On the other hand, the innermost layer is mostly constituted by inorganic compounds such as Li_3N covering the lithium metal, and delivering high Li-ion conductivity. In the DCA-based electrolyte, the SEI layer appears to be thicker with a very varied composition throughout its thickness. Nevertheless, it also contains $C=N$ polymeric components while its innermost layer is dominated by graphitic carbon and Li_3N/LiC_xH_yN species.

2.5. Study of DCA and TCM Mixed Electrolyte

In literature there are several examples of IL mixtures demonstrating the synergistic effects two different anions can bring for enhancement of ESW, SEI forming ability, and conductivity of the electrolyte.^[2,13,14,40–46] Therefore, an electrolyte containing LiDCA- Pyr_{14} TCM (1:9 molar ratio) was investigated to explore the occurrence of synergistic effects. With respect to conductivity and viscosity (see Figure 8a), unfortunately, synergies are not observed. In fact, while the viscosity decreases from 190 mPa s at 0 °C to 22 mPa s at 50 °C, lying in between those of the DCA- and TCM-based electrolytes, the ionic conductivity values (3.6 mS cm^{-1} at 0 °C, 4.9 mS cm^{-1} at 20 °C and, eventually, 13 mS cm^{-1} at 50 °C) are lower than any of the single anion electrolytes. Such unexpected behavior for conductivity can be attributed to stronger interactions among the ionic species with Li^+ when both anions are present.^[16]

Figure 8b reports the linear sweep voltammogram of the LiDCA- Pyr_{14} TCM electrolyte together, for the sake of comparison, with that of the LiTCM- Pyr_{14} TCM electrolyte. The anodic scan of LiDCA- Pyr_{14} TCM solution exhibits a behavior almost identical to the TCM-based electrolyte, which is not surprising considering that the majority of the solution consists of Pyr_{14} TCM. On the cathodic side, besides a small reduction peak at $\approx 1.7\text{ V}$ versus Li/Li^+ attributable to the DCA^- reduction, the overall trend is governed by the presence of TCM^- anion.

Figure 8c reports the voltage profile of a symmetrical Li cell employing LiDCA- Pyr_{14} TCM electrolyte subjected to the stripping/plating test. The initial overpotential is $\approx 40\text{ mV}$, i.e., only 5 mV higher than that of the TCM-based cell, but 50 mV lower than that of the DCA-based cell. Even more interesting is the trend upon extended cycling, in which the polarization increases only to 60 mV displaying a steady and flat voltage profile with respect to time. This suggests for a neat improvement of the Li/electrolyte interface resulting from the growth of a better performing SEI in the mixed electrolyte. This is further supported by the impedance spectra of Li electrode, shown in Figure 8d, recorded before and after extended cycling. Prior to cycling, the interfacial resistance in the cell was approx. $588\ \Omega\text{ cm}^2$, increasing to $\approx 910\ \Omega\text{ cm}^2$ after 84 cycles, which agrees with the polarization trend observed in the stripping/plating test.

For the practical application of lithium metal electrodes, stable cycling performance is also desired at higher current densities.^[47] Therefore, stripping/plating tests at increasing current density ($0.5, 1, 2,$ and 3 mA cm^{-2}) were performed on symmetrical Li cells employing LiDCA- Pyr_{14} TCM electrolyte (shown in Figure S8 in the Supporting Information). Stripping and plating current densities of equal magnitude were used for each experiment while the cycling time differed depending on the applied current density to have same amount of lithium deposit (0.05 mAh cm^{-2} per cycle) for all the measurements. At current density of 0.5 mA cm^{-2} (Figure S8a, Supporting Information) it was still possible to reversibly strip and plate lithium for 20 cycles, despite the increased overpotential. However, at higher currents the cells displayed a sudden overvoltage increase as early as the third cycle. This cell failure could be due to inhomogeneous deposition of lithium at high current. The high reactivity of the fresh generated lithium surface (presumably

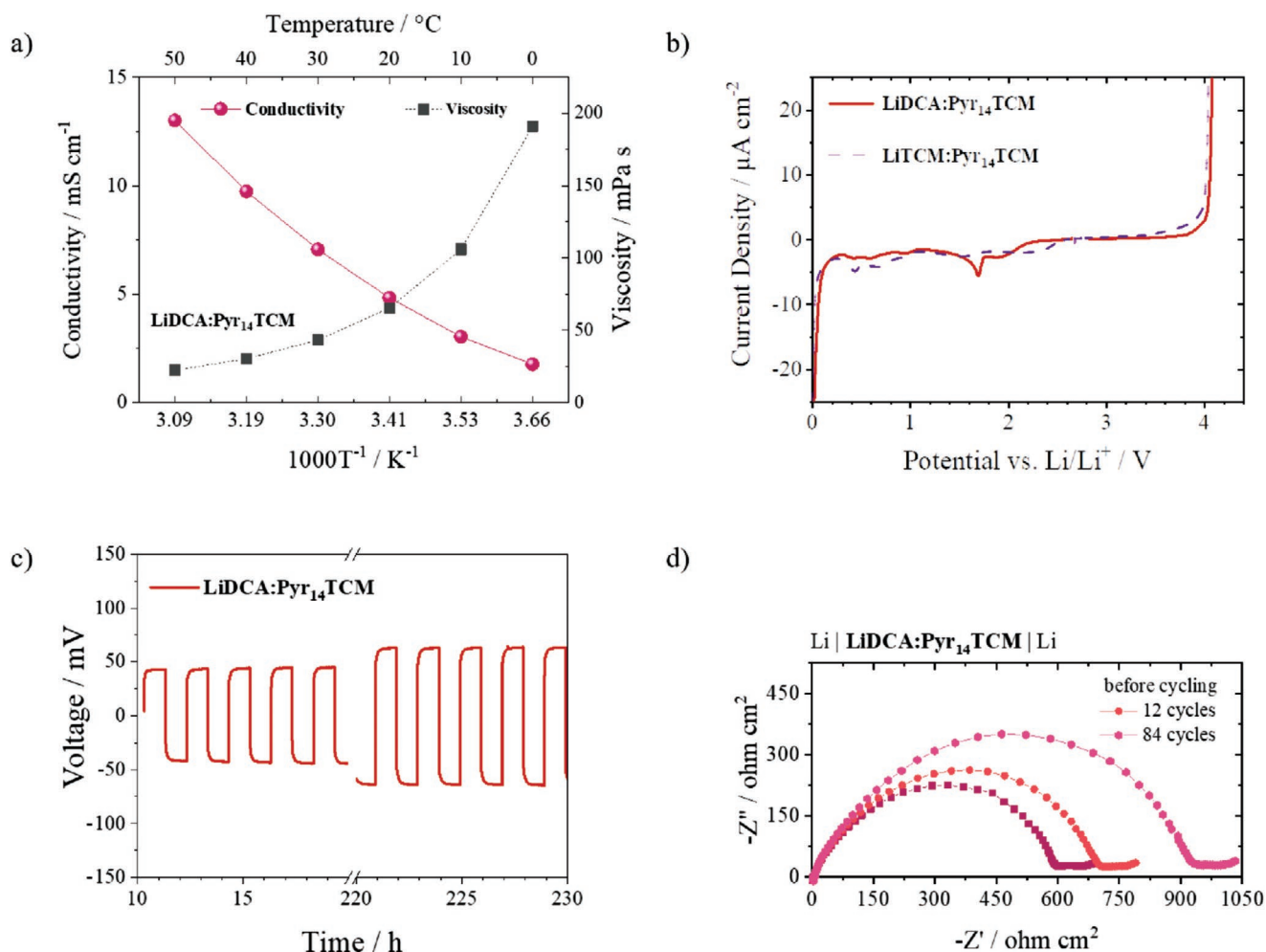


Figure 8. a) Ionic conductivity and viscosity versus temperature plots of LiDCA:Py_r₁₄TCM electrolytes in 1:9 mol salt:IL ratio; b) Linear sweep voltammograms of Li/IL/Pt cells recorded at scan rate of 1 mV s⁻¹ at 20 °C, LiDCA:Py_r₁₄TCM (red line) LiTCM:Py_r₁₄TCM (dashed purple); c) time evolution of the cell voltage during stripping/deposition measurements performed on a symmetrical Li/LiDCA:Py_r₁₄TCM/Li cell using a current of 0.05 mA cm⁻² and a deposition/stripping time of 1 h; d) Nyquist plots of the electrochemical impedance spectroscopy of a symmetrical Li/ LiDCA:Py_r₁₄TCM / Li upon time after 10 h rest prior to cycling, after 12 cycles and after 84 cycles.

with a relatively large area) may promote decomposition of the electrolyte, leading to rapid increase of cell impedance. Considering the growing interest on anode-free cells where Li is plated in-situ on the current collector upon the first charge, stripping and plating tests on nickel and copper foils were also performed and the corresponding Coulombic efficiencies calculated (as shown in Figure S9 in the Supporting Information). Coulombic efficiency was defined as the ratio of Li stripping capacity to Li plating capacity in each cycle which was limited to 0.1 mAh cm⁻². While the Coulombic efficiency of both cells appeared to be very low (≈40% for Ni foil), possibly due to inhomogeneous Li deposition and/or severe side reactions, the overvoltage in both cases was comparable to the stripping/plating test performed on symmetrical Li cell. In summary, further tuning of the electrolyte is certainly needed to enable its use in anode-free Li cells. However, it should be noted that this is particularly challenging even with conventional fluorinated electrolytes, mainly due to poor adhesion to the substrate and formation of mossy “dead” lithium.^[48]

2.5.1. SEI Composition in LiDCA-Py_r₁₄TCM Electrolyte

Due to similarities of the XPS results obtained for LiDCA-Py_r₁₄TCM with the TCM-based and DCA-based electrolytes, only the noteworthy remarks and differences are highlighted in Figure 9. Besides, the O 1s and Li 1s regions are shown in Figure S10 in the Supporting Information. As expected, the N 1s and C 1s photoelectrons regions of the outermost surface revealed the presence of species related to both DCA⁻ (–C–N⁻–C–) ($\Delta BE_{(N\ 1s-C\ 1s)} = 114.6 \pm 0.09$ eV) and TCM⁻ (–C≡N) ($\Delta BE_{(N\ 1s-C\ 1s)} = 113.3 \pm 0.09$ eV). In addition, the spectrum reveals the presence of two other features corresponding to single –C–N– bond and/or LiCHN ($\Delta BE_{(N\ 1s-C\ 1s)} = 111.2 \pm 0.1$ eV) and N=C– double bond ($\Delta BE_{(N\ 1s-C\ 1s)} = 114.6 \pm 0.05$ eV) in a polymeric network. The presence of the double bond is also testified by the observed π excitation signal toward higher BE (4 eV).

The overall shape of the spectra demonstrates the surface chemistry of the SEI formed in the mixed electrolyte to be very

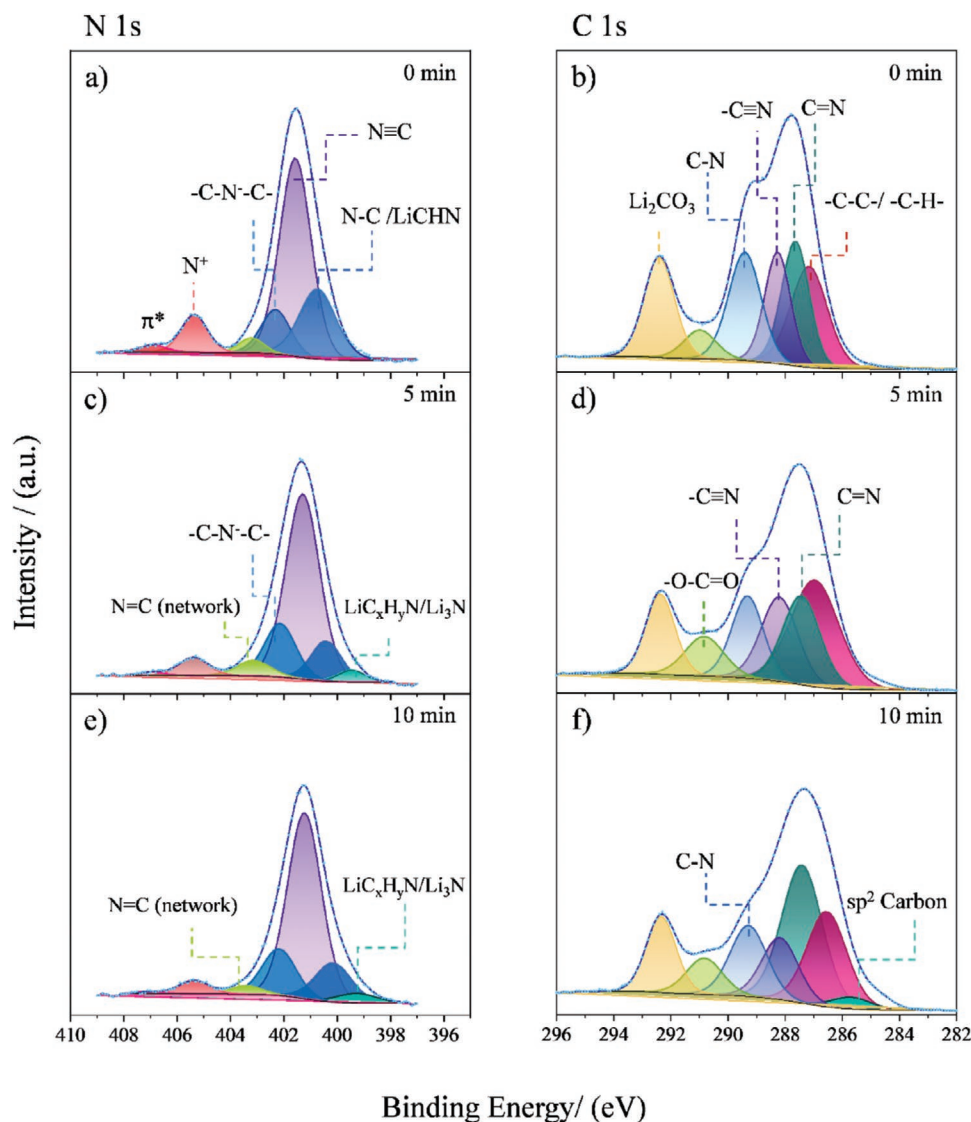


Figure 9. High-resolution N 1s and C 1s photoelectron spectra, before and after etching, of the Li metal surface after the first lithium plating cycle (current: 0.05 mA cm^{-2} , plating time 1 h) in LiDCA:Pyr₁₄TCM (1:9 mol:mol).

similar to that obtained in the TCM-based electrolyte. Upon 5 min of argon sputtering, the signatures of decomposition products including $-C-C-/-C-H-$ bonds in the C 1s region as well as $-C-N-$ bond and/or LiCHN in N 1s region increase. In addition, a new peak belonging to LiC_xH_yN/Li_3N in the N 1s region and sp^2 carbon in C 1s region appears. However, after 10 min of sputtering the overall composition of the SEI layer does not change significantly, only displaying an increase in the amount of the aforementioned decomposition products. This suggests the thickness of the SEI in the mixed electrolyte to be similar to that formed in the TCM-based electrolyte. Interestingly, the composition of the SEI layer formed in the mixed electrolyte appears to be more homogenous throughout its thickness (Figure S11, Supporting Information). Moreover, a lesser degree of graphitic carbon is formed in the mixed electrolyte, supporting our proposal regarding the crucial role of graphitic carbon in controlling the extent of the SEI layer growth.

3. Conclusion

In this study the physico-chemical and electrochemical characterization of LiDCA:Pyr₁₄DCA, LiTCM:Pyr₁₄TCM, and LiDCA:Pyr₁₄TCM (1:9 mol:mol ratio) as fluorine-free electrolytes for lithium metal batteries are reported. The investigation was extended to the SEI formed on Li metal within each electrolyte in terms of composition as well as evolution upon cycling. The results indicated significantly high ionic conductivity of about 5 mS cm^{-1} at room temperature as well as ESW of 4 V. The stripping/plating test performed with symmetrical Li cells showed the lowest overpotential for LiDCA:Pyr₁₄TCM (60 mV), and the highest for the LiDCA:Pyr₁₄DCA electrolyte (100 mV) indicating the formation of distinct SEIs with the different electrolytes.

According to the XPS results, the SEI formed in all three electrolytes were dominated by a polymer-rich layer including

carbon-nitrogen single, double and triple bonds. While in the TCM-based electrolyte the SEI appears to have a polymer-rich outermost layer and a more inorganic innermost layer, in the mixed electrolyte the SEI layer displayed a more homogenous composition throughout its thickness. In case of DCA-based electrolyte the SEI was mostly formed prior to cycling, as shown by the EIS results. The XPS experiments revealed that this spontaneously formed SEI contains sp^2 carbon in the inner layer, which plays a crucial role in favoring the SEI growth not blocking the electron transfer at the electrode/electrolyte interface. In agreement with the EIS results the system with the lowest interfacial resistance, i.e., LiDCA:Pyr₁₄TCM also displayed the least amount of sp^2 carbon in its SEI composition. The experimental results were also supported by the DFT and MD simulations.

Nonfluorinated IL electrolytes exhibit a great potential as safe, sustainable and relatively low-cost electrolyte for LMBs. However, their properties are not well known as their fluorinated counterparts. We believe that further in depth studies such as the present work, providing crucial insights into the electrochemical and interfacial properties of novel F-free electrolytes can definitively promote the development of more sustainable batteries.

4. Experimental Section

Electrolyte Preparation: 1-butyl-1-methylpyrrolidinium dicyanamide (Pyr₁₄DCA), 1-butyl-1-methylpyrrolidinium tricyanomethanide (Pyr₁₄TCM) as well as the Li salts, LiDCA and LiTCM were supplied by IoLiTec GmbH. ILs were initially dried at 40 °C, under moderate vacuum for 48 h (oil pump, $\leq 10^{-3}$ mbar) and subsequently under high vacuum for additional 48 h (turbo molecular pump, $\leq 10^{-7}$ mbar). The water content of the ILs was determined by coulometric Karl Fischer titration (Mettler-Toledo Titrator Compact C30) showing less than 20 ppm (detection limit 10 ppm). LiDCA and LiTCM were dried following the same two step drying procedure, but at 100 °C. All dried samples were directly transferred into an argon filled glove-box (LabMaster, Mbraun GmbH, Germany, O₂ < 0.1 ppm, H₂O < 0.1 ppm) for storage and cell assembly. The electrolyte solutions (salt:IL = 1:9 molar ratio) were prepared inside the glove-box.

Physicochemical Characterization: The ionic conductivity was determined by an automated conductimeter (MCS 10, BioLogic) equipped with a frequency analyzer and a thermostatic chamber. The ILs and the electrolyte solutions were housed (within the glove-box) in sealed glass conductivity cells (whose cell constant was determined to be $1.0 \pm 0.01 \text{ cm}^{-1}$ using a 0.01 mol L^{-1} KCl standard solution) equipped with two platinized platinum electrodes. The conductivity measurements were performed in the temperature range from 0 to 50 °C and back to 0 °C, with heating/cooling steps of 5 °C h⁻¹ followed by 2 h rest-step to reach equilibrium. Only a small hysteresis was observed for the conductivities measured upon heating and cooling, thus only the values collected during heating ramp are reported here.

Viscosity was measured using an Anton-Paar Physica MCR 301 rheometer. The shear rate used for all tests was 50 s⁻¹. The measurements were performed in the same temperature range as for conductivity, i.e., from 0 to 50 °C.

Electrochemical Tests: For the electrochemical characterization, three-electrode Swagelok cells were used. The cell assembly was carried out in an argon-filled glove box (LabMaster, Mbraun GmbH, O₂ < 0.1 ppm, H₂O < 0.1 ppm). For linear sweep voltammetry experiments (LSVs), a platinum electrode (diameter: 1 mm) was used as the working electrode (WE) and metallic lithium foil (99% battery grade, Honjo Metal, Japan) as counter and reference electrodes (CE and RE).

The electrochemical stability window of neat ILs and electrolytes was evaluated by linear sweep voltammetry (LSV). Each cathodic or anodic scan was measured on a freshly polished platinum electrode starting from the open circuit voltage (OCV) with scan rate of 1 mV s⁻¹ via a VMP-3 potentiostat (Biologic Science Instruments). Measurements were conducted at 20 ± 2 °C.

Stripping/plating tests were performed in symmetrical Li/electrolyte/Li cells hosted in CR2032 coin cell cases. These cells were cycled at current density of 0.05 mA cm⁻² (1 h for each step). Impedance spectra of these cells were recorded upon cycling every 24 h. The impedance spectra were collected at OCV in the frequency range of 1 MHz to 10 mHz, with the AC amplitude set to 5 mV.

X-ray Photoelectron Spectroscopy: XPS experiments were performed on the Li metal electrodes after the first lithium deposition cycle of Li symmetrical cells employing LiTCM-Pyr₁₄TCM, LiDCA-Pyr₁₄DCA, and LiDCA-Pyr₁₄TCM (1:9 mol:mol) electrolytes. The cells were disassembled inside the glove box, the electrodes rinsed with DMC and transferred to the XPS using an air-tight vessel to prevent their contact with air or moisture. For the measurements, the monochromatic Al K α ($h\nu = 1.487 \text{ eV}$) X-ray source and the Phoibos 150 XPS spectrometer (SPES—Surface Concept) equipped with a microchannel plate and delay line detector (DLD) were used. The scans were acquired in a fixed analyzer transmission mode with an X-ray source power of 200 W (15 kV), 30 eV pass energy, and 0.1 eV energy steps. The spectra were fitted with CasaXPS software, using a nonlinear Shirley-type background and 70% Gaussian and 30% Lorentzian profile functions. The position of the peaks was not calibrated due to the charging effects that shifted the peaks depending on the nature of the species, in other words, the shifts are inhomogeneous.^[49] However, the goodness of the peak fitting was carried out by determining the binding energy separations (Δ BEs) of each species observed in different elements, as was previously carried out for other Li-battery compounds.^[35]

Computational Details: Classic molecular simulations were performed with the Amber18 software package^[50] using the GAFF force field.^[51] Atomic charges were computed with Gaussian 09^[52] at the B3LYP/6-31+G* level of theory and applying the RESP^[51] algorithm. A multiplicative dielectric constant of 1.8 was used along the simulation since it was shown to return excellent agreement between experimental and computed densities in pure ionic liquids.^[53–55] The simulations consisted of a cubic box with ≈ 50 Å sides. More detailed information on the systems can be found in Table S3 (Supporting Information). The starting configuration was prepared with Packmol,^[56] then the simulation consisted of 10⁷ minimization cycles, 1 ns of NVT warming from 0 to 50 K, 20 ns of NPT equilibration at 300 K, 20 ns of NVT equilibration at 300 K, and finally an NVT production phase of 10 ns at 300 K. For all the phases a time step of 2 fs was used thanks to the SHAKE algorithm on light atoms. The final production phase was dumped every 1000 steps. The trajectories were analyzed using the TRAVIS^[8,9] software. DFT calculations were performed using the Gaussian 09 software at the B3LYP/6-31+G* level of theory. The starting guess geometry for the singlet clusters was hand-drawn using Avogadro^[57] and then optimized. The final equilibrium geometry of the singlet clusters was then used as the starting geometry of the doublet clusters. A frequency calculation on the final structures was employed to check that a true minimum of the potential energy surface was found, and no imaginary frequency was observed. From the frequency calculation the ZPE and the entropic contribution to the energy were also extracted. The results were analyzed with Avogadro and GaussView.

Supporting Information

Supporting Information is available from the Wiley Online Library or from the author.

Acknowledgements

This work was funded by the Bundesministerium für Bildung und Forschung (BMBF) with the project “NEILLSBAT” (Contract number

03XP0120A) within the M.Era-net framework. The authors also thank the Helmholtz Association for the financial support, as well as Dr. Boyan Iliiev and Dr. Thomas Schubert from Iolitec GmbH for providing the ionic liquids.

Open access funding enabled and organized by Projekt DEAL.

Conflict of Interest

The authors declare no conflict of interest.

Authors Contribution

S.P. supervised the work and provided funding. A.V. supervised the work, designed the experiments, and discussed the data. N.K. designed and carried out experiments, analyzed and discussed the data, and wrote the paper. M.Z. performed the XPS experiments, analyzed and discussed the data. A.M. carried out the computational simulations and wrote the simulation part. D.G. performed the physicochemical and electrochemical experiments. All authors reviewed the final version of the manuscript.

Keywords

ionic liquids, lithium metal batteries, nonfluorinated, solid electrolyte interphase, X-ray photoelectron spectroscopy

Received: November 9, 2020

Revised: December 1, 2020

Published online:

- [1] X. Zeng, M. Li, D. A. El-hady, W. Alshitari, A. S. Al-bogami, J. Lu, K. Amine, D. A. El-H, W. Alshitari, A. S. Al-bogami, J. Lu, K. Amine, *Adv. Energy Mater.* **2019**, 9, 1900161.
- [2] L. Grande, J. Von Zamory, S. L. Koch, J. Kalhoff, E. Paillard, S. Passerini, *ACS Appl. Mater. Interfaces* **2015**, 7, 5950.
- [3] A. Fericola, B. Scrosati, H. Ohno, *Ionics* **2006**, 12, 95.
- [4] H. Yoon, G. H. Lane, Y. Shekibi, P. C. Howlett, M. Forsyth, A. S. Best, D. R. MacFarlane, *Energy Environ. Sci.* **2013**, 6, 979.
- [5] G. B. Appetecchi, M. Montanino, D. Zane, M. Carewska, F. Alessandrini, S. Passerini, *Electrochim. Acta* **2009**, 54, 1325.
- [6] Y. Yoshida, O. Baba, G. Saito, *J. Phys. Chem. B* **2007**, 111, 4742.
- [7] D. R. MacFarlane, M. Forsyth, E. I. Izgorodina, A. P. Abbott, G. Annat, K. Fraser, *Phys. Chem. Chem. Phys.* **2009**, 11, 4962.
- [8] M. Brehm, B. Kirchner, *J. Chem. Inf. Model.* **2011**, 51, 2007.
- [9] M. Brehm, M. Thomas, S. Gehrke, B. Kirchner, *J. Chem. Phys.* **2020**, 152.
- [10] A. Mariani, L. Bencivenni, R. Caminiti, L. Gontrani, M. Campetella, C. Fasolato, F. Capitani, P. Postorino, C. Fasolato, M. Daniele, S. Lupi, R. Caminiti, *J. Mol. Liq.* **2017**, 226, 2.
- [11] W. Xu, C. A. Angell, *Science* **2003**, 302, 422.
- [12] W. Xu, L. M. Wang, R. A. Nieman, C. A. Angell, *J. Phys. Chem. B* **2003**, 107, 11749.
- [13] W. Xu, E. I. Cooper, C. A. Angell, *J. Phys. Chem. B* **2003**, 107, 6170.
- [14] D. R. MacFarlane, P. Meakin, J. Sun, N. Amini, M. Forsyth, *J. Phys. Chem. B* **1999**, 103, 4164.
- [15] M. Moreno, E. Simonetti, G. B. Appetecchi, M. Carewska, M. Montanino, G.-T. Kim, N. Loeffler, S. Passerini, *J. Electrochem. Soc.* **2017**, 164, A6026.
- [16] G. B. Appetecchi, M. Montanino, S. Passerini, *ACS Symp. Ser.* **2012**, 1117, 67.
- [17] D. R. MacFarlane, S. A. Forsyth, J. Golding, G. B. Deacon, *Green Chem.* **2002**, 4, 444.
- [18] D. R. MacFarlane, J. Golding, S. Forsyth, M. Forsyth, G. B. Deacon, *Chem. Commun.* **2001**, 16, 1430.
- [19] R. C. Beaumont, K. B. Aspin, T. J. Demas, J. H. Hoggatt, G. E. Potter, *Inorg. Chim. Acta* **1984**, 84, 141.
- [20] E. Markevich, V. Baranchugov, G. Salitra, D. Aurbach, M. A. Schmidt, *J. Electrochem. Soc.* **2008**, 155, A132.
- [21] P. C. Howlett, D. R. MacFarlane, A. F. Hollenkamp, *Electrochem. Solid-State Lett.* **2004**, 7, A97.
- [22] V. Borgel, E. Markevich, D. Aurbach, G. Semrau, M. Schmidt, *J. Power Sources* **2009**, 189, 331.
- [23] H. Matsumoto, H. Kageyama, Y. Miyazaki, *Electrochemistry* **2003**, 71, 1058.
- [24] J.-H. Shin, W. A. Henderson, S. Passerini, *J. Electrochem. Soc.* **2005**, 152, A978.
- [25] J. P. Hoffknecht, M. Drews, X. He, E. Paillard, *Electrochim. Acta* **2017**, 250, 25.
- [26] C. Liu, X. Ma, F. Xu, L. Zheng, H. Zhang, W. Feng, X. Huang, M. Armand, J. Nie, H. Chen, Z. Zhou, *Electrochim. Acta* **2014**, 149, 370.
- [27] V. L. Martins, A. J. R. Rennie, R. M. Torresi, P. J. Hall, *Phys. Chem. Chem. Phys.* **2017**, 19, 16867.
- [28] S. Bhattacharyya, J. Hong, G. Turban, *J. Appl. Phys.* **1998**, 83, 3917.
- [29] S. Bhattacharyya, C. Cardinaud, G. Turban, *J. Appl. Phys.* **1998**, 83, 4491.
- [30] A. P. Dementjev, A. De Graaf, M. C. M. Van de Sanden, K. I. Maslakov, A. V. Naumkin, A. A. Serov, *Diam. Relat. Mater.* **2000**, 9, 1904.
- [31] M. Ricci, M. Trinquocoste, F. Auguste, R. Canet, P. Delhaes, C. Guimon, G. Pfister-Guillouzo, B. Nysten, J. P. Issi, *J. Mater. Res.* **1993**, 8, 480.
- [32] F. Rossi, B. Andre, A. van Veen, P. E. Miinarends, H. Schut, F. Labohm, H. Dunlop, M. P. Delnlancke, K. Hubbard, *J. Mater. Res.* **1994**, 9, 2440.
- [33] F. Buchner, K. Forster-Tonigold, M. Bozorgchenani, A. Gross, R. J. Behm, *J. Phys. Chem. Lett.* **2016**, 7, 226.
- [34] P. C. Howlett, N. Brack, A. F. Hollenkamp, M. Forsyth, D. R. MacFarlane, *J. Electrochem. Soc.* **2006**, 153, A595.
- [35] K. N. Wood, G. Teeter, *ACS Appl. Energy Mater.* **2018**, 1, 4493.
- [36] F. Buchner, M. Bozorgchenani, B. Uhl, H. Farkhondeh, J. Bansmann, R. J. Behm, *J. Phys. Chem. C* **2015**, 119, 16649.
- [37] H. Zhang, X. Judez, A. Santiago, M. Martinez-Ibañez, M. Á. Muñoz-Márquez, J. Carrasco, C. Li, G. G. Eshetu, M. Armand, *Adv. Energy Mater.* **2019**, 9, 1900763.
- [38] J. P. Paraknowitsch, J. Zhang, D. Su, A. Thomas, M. Antonietti, *Adv. Mater.* **2010**, 22, 87.
- [39] B. Guo, X. G. Sun, G. M. Veith, Z. Bi, S. M. Mahurin, C. Liao, C. Bridges, M. P. Paranthaman, S. Dai, *Adv. Energy Mater.* **2013**, 3, 708.
- [40] T. J. Wooster, K. M. Johanson, K. J. Fraser, D. R. MacFarlane, J. L. Scott, *Green Chem.* **2006**, 8, 691.
- [41] T. P. Fellinger, D. S. Su, M. Engenhorst, D. Gautam, R. Schlögl, M. Antonietti, *J. Mater. Chem.* **2012**, 22, 23996.
- [42] A. Wang, C. Wang, L. Fu, W. Wong-Ng, Y. Lan, *Nano-Micro Lett.* **2017**, 9, 47.
- [43] G.-T. Kim, T. Kennedy, M. Brandon, H. Geaney, K. M. Ryan, S. Passerini, G. B. Appetecchi, *ACS Nano* **2017**, 11, 5933.
- [44] G. B. Appetecchi, M. Montanino, A. Balducci, S. F. Lux, M. Winterb, S. Passerini, *J. Power Sources* **2009**, 192, 599.
- [45] A. P. Lewandowski, A. F. Hollenkamp, S. W. Donne, A. S. Best, *J. Power Sources* **2010**, 195, 2029.
- [46] G. H. Lane, A. S. Best, D. R. MacFarlane, A. F. Hollenkamp, M. Forsyth, *J. Electrochem. Soc.* **2010**, 157, A876.

- [47] P. Albertus, S. Babinec, S. Litzelman, A. Newman, *Nat. Energy* **2018**, 3, 16.
- [48] S. S. Zhang, X. Fan, C. Wang, *Electrochem. Commun.* **2018**, 89, 23.
- [49] G. Ferraresi, L. Czornomaz, C. Villevieille, P. Novák, M. E. I. Kazzi, *ACS Appl. Mater. Interfaces* **2016**, 8, 29791.
- [50] D. A. Case, T. E. Cheatham, T. Darden, H. Gohlke, R. Luo, K. M. Merz, A. Onufriev, C. Simmerling, B. Wang, R. J. Woods, *J. Comput. Chem.* **2005**, 26, 1668.
- [51] J. Wang, R. M. Wolf, J. W. Caldwell, P. A. Kollman, D. A. Case, *J. Comput. Chem.* **2004**, 25, 1157.
- [52] M. J. Frisch, M. J. Trucks, G. W. Schlegel, H. B. Scuseria, G. E. Robb, M. A. Cheeseman, J. R. Scalmani, G. Barone, V. Petersson, G. A. Nakatsuji, et al., Gaussian 09, Revision A.02, Gaussian, Inc., Wallingford CT **2016**.
- [53] A. Mariani, R. Caminiti, M. Campetella, L. Gontrani, *Phys. Chem. Chem. Phys.* **2016**, 18, 2297.
- [54] A. Mariani, R. Caminiti, L. Gontrani, *Phys. Chem. Chem. Phys.* **2017**, 19, 8661.
- [55] M. Campetella, A. Mariani, C. Sadun, B. Wu, E. W. Castner, L. Gontrani, *J. Chem. Phys.* **2018**, 148, 134507.
- [56] L. Martínez, R. Andrade, E. G. Birgin, J. M. Martínez, *J. Comput. Chem.* **2009**, 30, 2157.
- [57] M. D. Hanwell, D. E. Curtis, D. C. Lonie, T. Vandermeersch, E. Zurek, G. R. Hutchison, *J. Cheminform.* **2012**, 4, 17.